Enhancing molecular oxygen activation by nitrogen-doped carbon encapsulating FeNi alloys with ultra-low Pt loading

Dandan Zhu[a,b], Yu Huang [ID][a,b,*], Xianjin Shi [ID][a,b], Rong Li[a,b], Zhenyu Wang[a,b], Wei Peng[a,b], Junji Cao[c] and Shuncheng Lee[d]

[a]Key Laboratory of Aerosol Chemistry and Physics, State Key Laboratory of Loess and Quaternary Geology (SKLLQG), Institute of Earth Environment, Chinese Academy of Sciences (CAS), Xi'an 710061, China
[b]Center for Excellence in Quaternary Science and Global Change, Chinese Academy of Sciences, Xi'an 710061, China
[c]Institute of Atmospheric Physics, Chinese Academy of Sciences, Beijing 100029, China
[d]Thrust of Earth, Ocean and Atmospheric Sciences Function Hub, The Hong Kong University of Science and Technology (Guangzhou), Guangzhou 511453, China
*To whom correspondence should be addressed: Email: huangyu@ieecas.cn
Edited By Levi Thompson

Abstract

Modulating the electronic structure of noble metals via electronic metal–support interaction (EMSI) has been proven effectively for facilitating molecular oxygen activation and catalytic oxidation reactions. Nevertheless, the investigation of the fundamental mechanisms underlying activity enhancement has primarily focused on metal oxides as supports, especially in the catalytic degradation of volatile organic compounds. In this study, a novel Pt catalyst supported on nitrogen-doped carbon encapsulating FeNi alloy, featuring ultrafine Pt nanoparticles, was synthesized. This catalyst demonstrated exceptional catalytic activity (92%), recyclability, and water tolerance for the deep oxidation of formaldehyde at room temperature. Structural analyses and theoretical calculations revealed a directional electron transfer from FeNi alloy to Pt, even there is no direct contact between them. This electron penetration effect, mediated by carbon, conferred electron-rich properties to Pt, leading to the activation of molecular oxygen by elongating O–O bond length (1.405 Å). Consequently, efficient formaldehyde removal was achieved with an ultra-low Pt loading. This investigation offers a novel perspective on modulating the electronic structure of Pt by engineering a unique EMSI effect between a nonoxide support and active species, thereby enabling efficient oxygen activation for air purification.

Keywords: FeNi alloy, ultra-low Pt loading, molecular oxygen activation, electronic metal–support interaction

Significance Statement

Molecular oxygen activation is one of the core issues in catalytic oxidation process. Although modulating the electronic structure of noble metals via electronic metal–support interaction has been proven effectively for facilitating oxygen activation, the exploration of the fundamental principles behind it has primarily been restricted to metal oxides as supports, particularly in catalytic oxidation of volatile organic compounds (VOCs). A novel Pt catalyst supported on nitrogen-doped carbon encapsulating FeNi alloy was developed and demonstrated exceptional catalytic activity (92%) for deep oxidation of formaldehyde, a carcinogenic indoor VOC. This work presents a promising strategy to modulate the electronic structure of Pt by directional electron transfer from FeNi alloy to Pt through carbon, enabling efficient oxygen activation for air purification.

Introduction

Supported noble metal catalysts have attracted considerable attention as a kind of heterogeneous catalyst in the fields of environmental remediation (1), chemical synthesis (2), and energy conversion (3). Particularly, the noble metal nanoparticles (NPs), such as Pt^0 and Pd^0, have been proven to be the most efficient active centers in catalytic degradation of volatile organic compounds (VOCs) owing to their strong ability toward molecular oxygen (O_2) activation, which is a critical step in catalytic oxidation

process (4–7). It is noteworthy that the charge transfer between the noble metal and O_2 molecule strongly relies on the electronic structure of the former (8, 9). Considerable efforts have been directed toward optimizing the electronic properties of noble metals with the aim of reducing their content while preserving their catalytic activity. This can be exemplified by the removal of formaldehyde (HCHO), a carcinogenic indoor air pollutant, using supported Pt catalysts (10, 11). Nevertheless, the practical application of these catalysts has been hindered by the scarcity and high cost

of precious metals. Consequently, the precise modulation of the electronic structure of noble metals to further enhance their intrinsic activity in oxygen activation remains of paramount importance for maximizing their utilization.

Recent studies have demonstrated the effective tuning of oxygen activation and catalytic properties in noble metal-based catalysts through the engineering of electronic interactions between the noble metal and the support (9, 12–14). For instance, partial electron transfer from Co_3O_4 to Pt NPs can generate electron-rich Pt, which enhances O_2 activation and facilitates toluene oxidation (13). Similarly, the electron donation from reduced TiO_2 to Pd can confer a negative charge to Pd NPs, thereby promoting oxygen dissociation and HCHO oxidation (9). However, the manipulation of the electronic structure of noble metals via electronic metal–support interaction (EMSI) and the exploration of the fundamental principles behind it have primarily been restricted to the employment of metal oxides as supports, particularly in catalytic oxidation of VOCs (13, 15). Basically, the critical role of support is embodied from its stabilization for supported metals and the modulation in the electronic structure of active metals. In view of this, carbon-based materials have been regarded as ideal nonoxide supports for anchoring Pt NPs due to their high conductivity and porous structure (16, 17). Nevertheless, the employment of promoters, such as alkali metals, is essential for attaining the high catalytic performance required for indoor air pollution control, primarily due to the weak metal–support interaction between the carbon substrate and the active species (17). Notably, the strong coupling between the *d* orbitals of transition metals (TMs) and the *p* orbitals of carbon facilitates the efficient transfer of electrons from TMs to carbon materials, particularly when forming nitrogen-doped carbon (NC) encapsulated TMs NPs (TMs@NC) (18–20). Furthermore, electron transfer can be achieved from the TMs core to the loaded Pt NPs through carbon, thanks to their distinct work functions (21). This phenomenon induces enhanced EMSI between the substrate and Pt NPs, thereby increasing the electron density of Pt. For instance, Li et al. utilized Co/NC heterojunctions as "solid-ligands" to stabilize and activate ultrafine Pt NPs, resulting in a substantial enhancement in the mass activity of Pt for hydrogen evolution (21). Deng et al. demonstrated the electron penetration from CoNi to Pt NPs and Pt-graphene interface, which facilitated O_2 activation at the Pt–graphene interface for CO oxidation, despite the saturated Pt sites by CO (22). To the best of our knowledge, the facilitation of molecular oxygen activation on electron-rich Pt through coupling the Pt NPs with TMs@NC has rarely been studied, making it meaningful to adopt this strategy to exploit the efficient Pt catalyst with ultra-low loading.

In this study, we devised a novel supported Pt catalyst (FeNi@NC/Pt) by integrating ultrafine Pt NPs with NC encapsulating FeNi alloy (FeNi@NC). This unique catalyst structure was employed to investigate its advantageous influence on the activation of molecular oxygen. Firstly, the carbon layer covering the FeNi alloy NPs serves as a protective shield, preventing the oxidation of metallic FeNi. Secondly, the intertwined nitrogen-doped carbon nanotubes (CNTs) derived from carbon-containing precursors, catalyzed by metallic Fe and Ni during high-temperature pyrolysis, ensure an ample supply of anchoring sites for Pt dispersion. Most importantly, the directional transfer of electrons from the FeNi alloy to Pt through NC results in an increased electron density on Pt NPs. As a consequence, the activation of molecular oxygen is significantly augmented by the electron-rich Pt, attributable to the EMSI effect between the nonoxide support and Pt. This enhancement leads to efficient oxidation of HCHO even at ultra-low Pt loading.

Results

Synthesis and physical structure

To stabilize Pt NPs on carbon substrate, the FeNi@NC support was constructed through one-step pyrolysis of the mixed $Ni_3[Fe(CN)_6]_2$ and $g-C_3N_4$ precursors that were validated by X-ray diffraction (XRD) (Figs. 1A and S2). A scanning electron microscopy image shows that the interlaced CNTs throughout FeNi@NC endow it a three-dimensional structure (Fig. S3), affording abundant anchor sites for Pt NPs and transfer channels for reactants. XRD pattern in Fig. 1B displays that FeNi@NC exhibits three diffraction peaks at 2θ of 44.0°, 51.3°, and 75.3°, being similar to those of the face-centered cubic (*fcc*) Ni (JCPDS no. 04-0850) (23, 24). The negative shift in diffraction peaks relative to those of the standard Ni sample may be caused by the formation of FeNi alloy owing to the entrance of larger Fe atoms into the crystal lattice of *fcc* Ni phase (25). The weak peak assigned to the (002) plane of graphitic carbon is observed at around 26°, which is derived from the carbon-containing precursors catalyzed by metallic Fe and Ni at high temperature (26). Transmission electron microscopy (TEM) and high-resolution TEM (HRTEM) observations further reveal that the FeNi alloy NPs are encapsulated by nanotubes, where two sets of lattice fringes with *d*-spacing of 0.205 and 0.340 nm are assigned to the (111) plane of FeNi alloy and (002) plane of graphitic carbon, respectively (Fig. 1C and D) (27, 28).

After loading of Pt NPs on support, the as-obtained FeNi@NC/Pt catalyst presents the identical XRD pattern to that of FeNi@NC, suggesting that the modification of Pt does not pose any effect on the phase structure of support. Although any signal related to Pt species is not detected in the XRD spectrum, the ultrafine Pt particles (2–4 nm) could be observed in Fig. 1E–G (red circle), with the interplanar spacing of 0.228 nm for identifying the (111) plane of metallic Pt (29). The actual content of Pt was determined to be 0.0694 wt.% by inductively coupled plasma-atomic emission spectrometry (ICP-AES). This ultra-low Pt loading avoids its agglomeration on carbon matrix. Noticeably, Pt NPs do not contact directly with FeNi alloys beneath carbon, hinting that the probable interaction between FeNi alloys and Pt NPs might be mediated by the graphitic carbon with high conductivity. The coexistence and uniform distribution of metal species could also be revealed by a high-angle annular dark-field scanning transmission electron microscopy (HAADF-STEM) image and the elemental mappings (Fig. 1H), where the larger and smaller bright spots are attributed to FeNi alloys and Pt NPs, respectively. The complete overlap of Ni and Fe verifies the formation of FeNi alloys at atomic level, echoing the results of XRD. In addition, the texture structures of FeNi@NC and FeNi@NC/Pt were evaluated by N_2 adsorption–desorption experiments (Fig. S4A and B). These samples exhibit the type IV isotherms with H3 hysteresis loops, indicating their evident mesoporous structures around 2.3 nm (Fig. S4D). The similar specific surface area (S_{BET}) and pore width distribution of FeNi@NC and FeNi@NC/Pt manifest that the loaded Pt NPs pose a marginal effect on the texture features. Based on the comprehensive results of the above characterizations, it can be concluded that the ultrafine Pt NPs are successfully anchored on CNTs encapsulating FeNi alloys. Then, another two Pt catalysts with nearly equivalent Pt loading (~0.065 wt.%) were prepared by using the Fe NPs-embedded NC microspheres (Fe@NC) (Fig. S5) and commercial carbon black (CB) (Fig. S6) as supports, respectively, for elucidating the structural advantage of FeNi@NC/Pt in the following section.

Catalytic activity and stability

The catalytic activity toward HCHO oxidation was evaluated in a continuous-flow reactor. From Fig. 2A, one can see that an evident
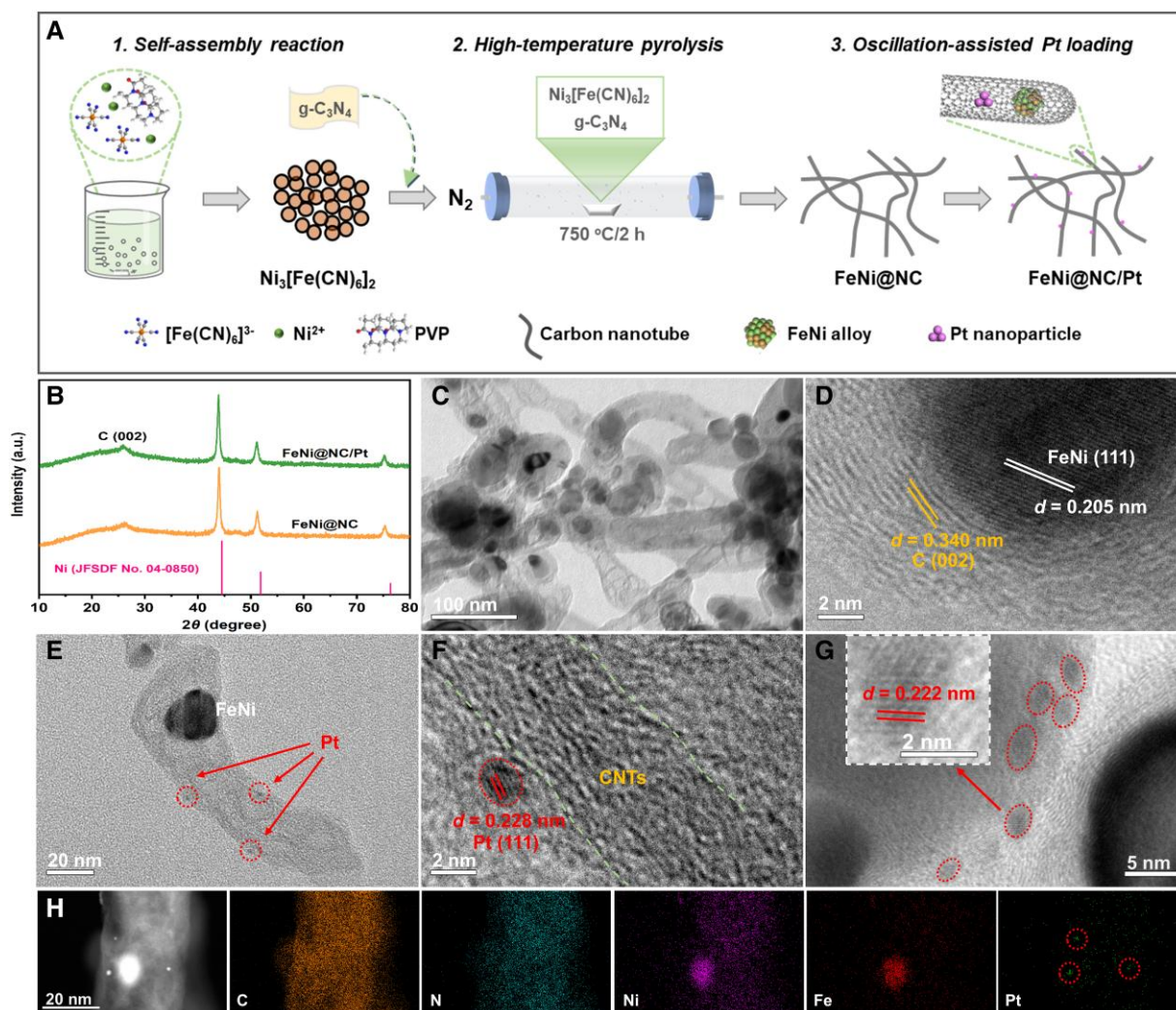
Fig. 1. Synthesis and structural characterization of FeNi@NC and FeNi@NC/Pt. A) Synthetic diagram of Ni$_3$[Fe(CN)$_6$]$_2$, FeNi@NC, and FeNi@NC/Pt. B) XRD patterns of FeNi@NC and FeNi@NC/Pt. TEM and HRTEM images of C and D) FeNi@NC and E–G) FeNi@NC/Pt. H) HAADF-STEM image and the elemental mappings of C, N, Ni, Fe, and Pt for FeNi@NC/Pt.

deactivation occurs over FeNi@NC as a function of time, while FeNi@NC/Pt exhibits an excellent and stable catalytic activity, with 92% of HCHO eliminated after 60 min of testing, indicating that the loading of Pt NPs is indispensable to achieve efficient HCHO abatement. Fe@NC- and CB-supported Pt catalysts (Fe@NC/Pt and CB/Pt) were also adopted to remove HCHO at the identical conditions, among which Fe@NC/Pt possesses the similar catalytic capacity to FeNi@NC/Pt, while CB/Pt exhibits a relatively lower removal efficiency despite its larger S_{BET} (Fig. S4C). These results imply that the TM NPs encased by carbon play a critical role in HCHO oxidation. The similar trends of CO$_2$ generation to HCHO removal also support this speculation (Fig. S7). To illustrate the advantage of FeNi@NC as a support compared with Fe@NC and CB, the actual and theoretical Pt contents in different catalysts are shown in Fig. 2B. Although the actual Pt loadings determined by ICP-AES are smaller than the nominal values owing to the inevitable losses during catalyst preparation (30), the Pt utilization of FeNi@NC/Pt is much higher than that of Fe@NC/Pt and CB/Pt. This phenomenon suggested that the interlaced CNTs network in FeNi@NC could provide numerous anchor sites for Pt deposition, thus presenting a higher utilization of Pt source than others. Further, the contribution of FeNi core to HCHO oxidation

was studied by reducing Pt loadings in the serial FeNi@NC/Pt and CB/Pt catalysts. As shown in Fig. 2C, the catalytic activity of FeNi@NC/Pt diminishes slightly with the decrease of Pt content, while the HCHO removal efficiency of CB/Pt decreases more obviously when reducing Pt content (Fig. 2D). The excellent HCHO oxidation activity of FeNi@NC/Pt may originate from the EMSI between FeNi@NC and Pt, thereby behaving the ultra-low Pt loading in comparison with the state-of-art Pt catalysts for HCHO removal, especially in the continuous-flow mode (8, 11, 17, 31–33). Specifically, the comparison of HCHO abatement between FeNi@NC/Pt and the reported Pt-based catalysts is shown in Fig. 2E and Table S1. One can see that the catalytic activity decreases significantly when reducing Pt loadings in previous catalyst systems, such as Pt/TiO$_2$-IMP-NaBH$_4$ (1 and 2), Pt/P25 (DP-HCHO) (4 and 5), Pt/ZnO/TiNT (6 and 7), Pt-NC and Pt-Mix (11 and 12), and Na–Pt/AC (13 and 14). Conversely, 84% of removal efficiency could be retained even with 0.0338 wt.% Pt loading in our catalyst system, further revealing the structural advantage of FeNi@NC/Pt. Subsequently, the recycling and water tolerance experiments were conducted to explore the potential of FeNi@NC/Pt for practical application. As depicted in Fig. 2F, the profile of HCHO removal remains almost unchanged after five
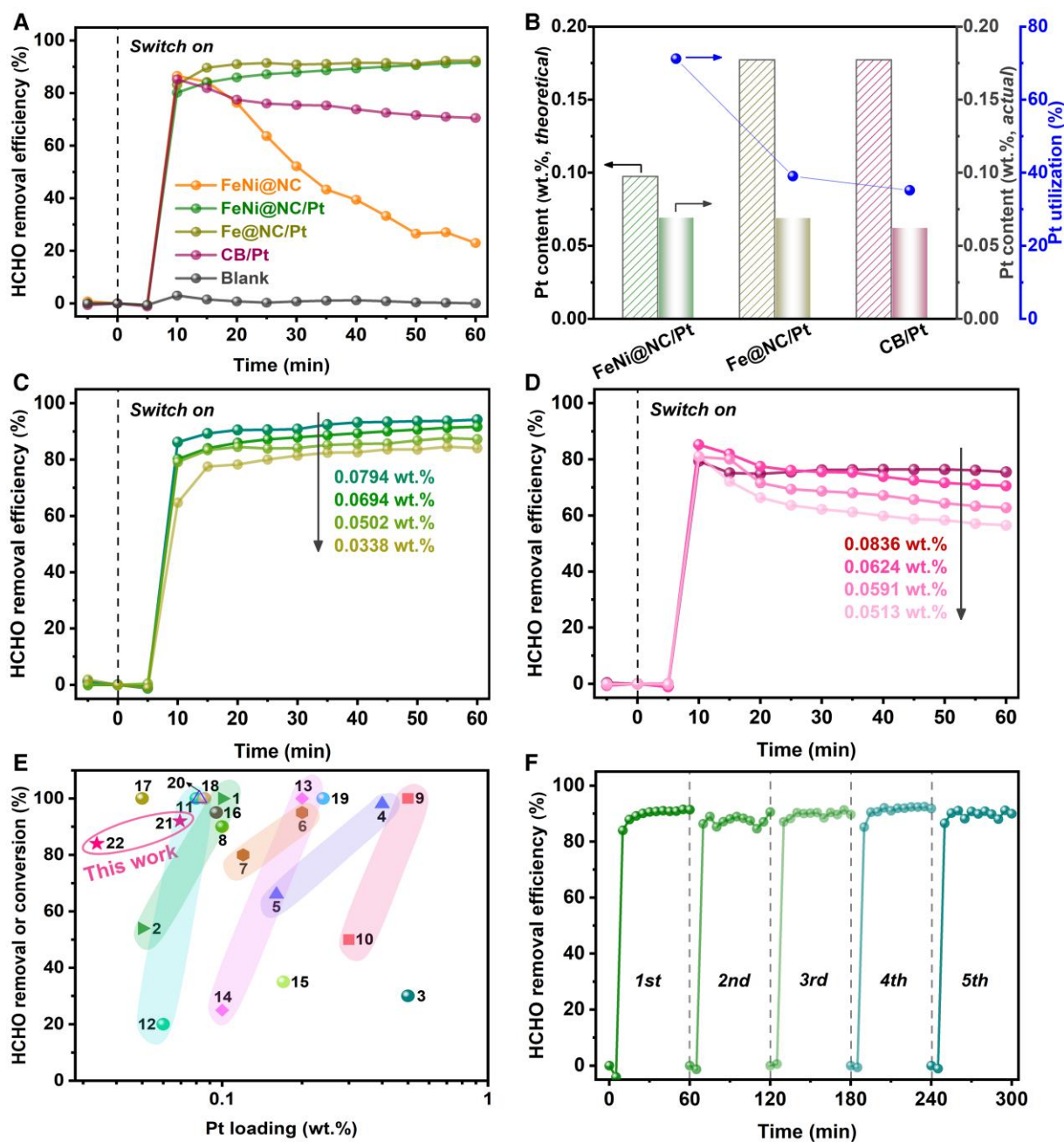
Fig. 2. Catalytic performance of HCHO oxidation. A) HCHO removal efficiency over different catalysts. B) The theoretical and actual contents, and utilization of Pt over FeNi@NC/Pt, Fe@NC/Pt, and CB/Pt. HCHO removal efficiency over C) FeNi@NC/Pt and D) CB/Pt with different Pt loadings. E) Comparison of catalytic activity between FeNi@NC/Pt and the reported Pt-based catalysts with Pt loadings no more than 0.5 wt.% tested in the continuous-flow mode. Detailed information is given in Table S1. F) Recycling tests of FeNi@NC/Pt. Reaction conditions: 100 ppm of HCHO in air, ~30% RH, and a GHSV of 60,000 mL g^{-1} h^{-1}.

cycles of testing. The catalytic activity maintains above 90% in the relative humidity (RH) ranging from 30 to 75%, suggesting that water does not influence the catalytic property in the wide RH range (Fig. S8). Besides, this catalyst could retain high activity for 15 h under both high and low concentrations of HCHO at room temperature (Figs. S9 and S10). The excellent catalytic activity, stability, and water tolerance declare the huge potential of FeNi@NC/Pt for practical application.

Chemical states and electronic structure

Although the above analyses have attested to the beneficial effect of FeNi@NC, especially FeNi alloys, on HCHO oxidation, the

in-depth exploration still needs to make for clarifying the origin of high activity exhibited by FeNi@NC/Pt. X-ray photoelectron spectroscopy (XPS) was initially adopted to analyze the surface compositions and chemical states of samples. The survey spectra show the coexistence of Ni, Fe, O, N, and C in FeNi@NC and FeNi@NC/Pt (Fig. S11), with the element contents listed in Table 1 except for Fe. One can see that both the support and catalyst are mainly composed of C and N, which are derived from the carbon and nitrogen sources of the mixed precursors, whereas the oxygen with relatively lower contents is originated from the surface oxygen species. The undetectable atomic percent of Fe might be caused by its insertion into the crystal lattice of cubic Ni, making it

difficult to measure by XPS with a detection limit. The absence of Pt signal in the survey spectrum of FeNi@NC/Pt is attributed to its quite low loading, being validated by the results of XRD and ICP-AES. High-resolution XPS spectra of Ni 2p and Fe 2p are displayed in Fig. 3A and D to discuss the chemical states of metal species. Figure 3A shows the signals of Ni $2p_{3/2}$ and Ni $2p_{1/2}$, which are deconvoluted into two pairs of peaks at around 852.9/870.5 and 854.6/872.2 eV, corresponding to Ni^0 and Ni^{2+}, respectively (23, 34). The signals at 860.7 and 879.2 eV are assigned to the characteristics of satellite peaks (27, 35). In comparison with FeNi@NC, a marginally positive shift in binding energy could be discovered at Ni $2p_{3/2}$ orbital of Ni^0 in FeNi@NC/Pt, suggesting that a possible electron transfer occurs from FeNi to Pt mediated by carbon. The existence of Ni^{2+} signal might originate from the unavoidable

surface oxidation of Ni^0 underlying the porous carbon. Nonetheless, the undetectable signals related to any metal oxides in XRD pattern suggest that the surface oxidation is quite weak. The almost equal Ni^0/Ni^{2+} ratios of FeNi@NC and FeNi@NC/Pt could verify the protection of carbon layer, which can not only guarantee the electron transfer between FeNi and Pt owing to the high conductivity, but also prevent the FeNi cores from further oxidizing during Pt loading. Moreover, Ar^+ sputtering was adopted during XPS measurements to identify the main component of Ni species in FeNi@NC/Pt (Fig. S12). The intensity of Ni^0 signal increases gradually with the sputtering time, accompanied by the shrinkage of Ni^{2+} peak, indicating that Ni is dominant by metallic state. High-resolution Fe 2p spectra show that the difference in binding energy between the main peak at Fe $2p_{3/2}$ and Fe $2p_{1/2}$ orbitals is 13.2 eV, implying that Fe^0 is the main Fe species (Fig. 3D). The appearance of Fe^{2+} is caused by the surface oxidation, being similar to Ni species (Fig. S13) (36).

X-ray absorption fine structure (XAFS) spectroscopy was further performed to analyze the electronic property and atomic structure of FeNi@NC/Pt. As shown in Fig. 3B and E, FeNi@NC/Pt exhibits roughly similar Ni and Fe K-edge X-ray absorption near-edge structure (XANES) profiles to those of the Ni and Fe foils, respectively, implying that both Ni and Fe species are dominant by their metallic states. Nonetheless, compared with Ni foil, the

Table 1. Element contents and molar ratios determined from XPS data.

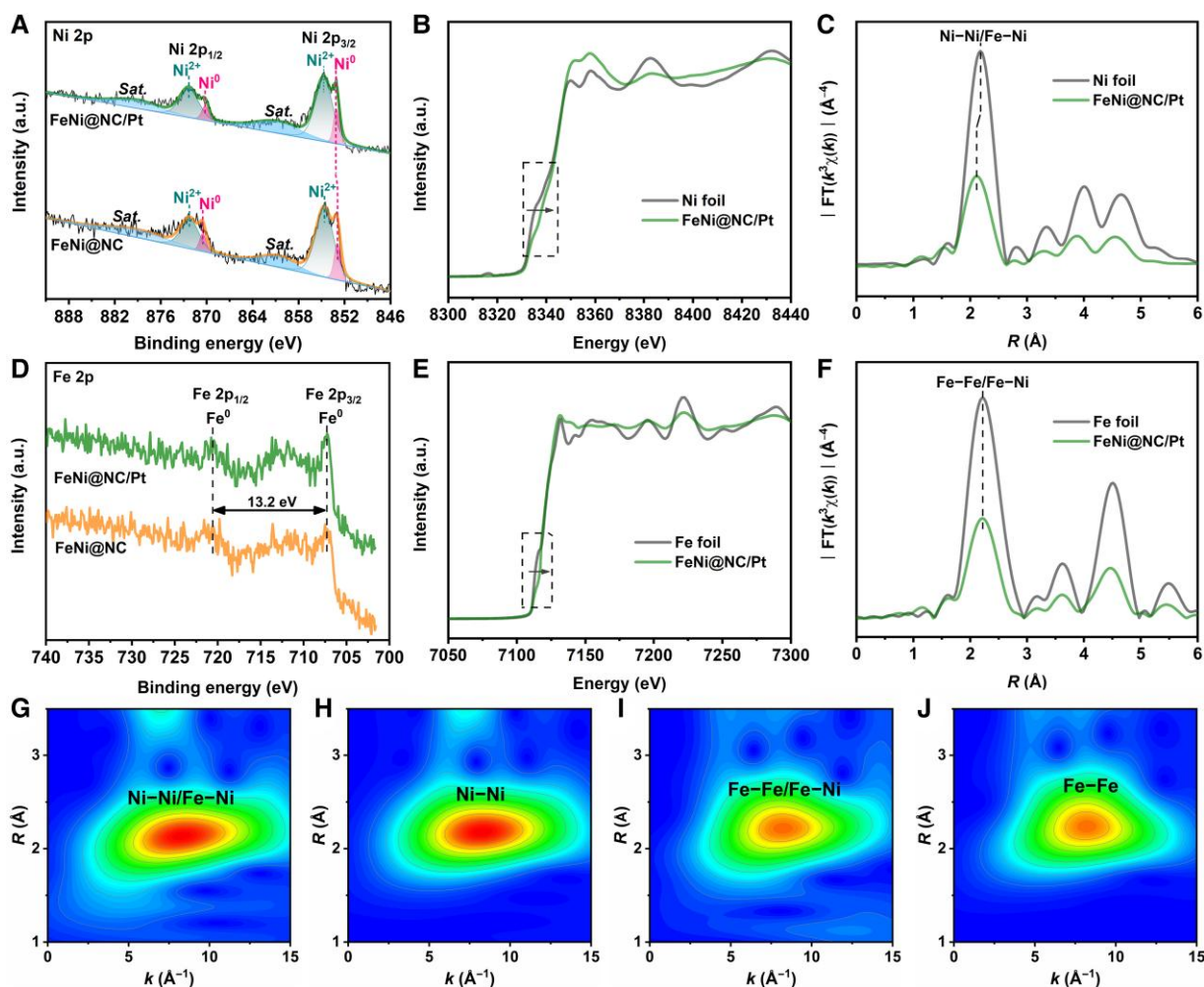| Samples	C at.%	N at.%	O at.%	Ni at.%	Ni^0/Ni^{2+} ratio	$(O_{Oads/C=O})/O_{total}$ %	$C_{C=O}/C_{total}$ %
FeNi@NC	90.80	4.95	3.32	0.93	0.184	42.90	10.24
FeNi@NC/Pt	90.40	5.69	3.21	0.70	0.185	54.22	10.35

Fig. 3. Chemical states and electronic structure. High-resolution XPS spectra of A) Ni 2p and D) Fe 2p for FeNi@NC and FeNi@NC/Pt. The normalized B) Ni and E) Fe K-edge XANES spectra of FeNi@NC/Pt. Fourier transformed k^3-weighted C) Ni and F) Fe K-edge EXAFS data for FeNi@NC/Pt. Wavelet transformed spectra of G and I) FeNi@NC/Pt, H) Ni foil, and J) Fe foil.

preedge absorption of Ni in FeNi@NC/Pt has a slight shift toward the higher energy, accompanied by the relatively higher intensity in the white line peak, indicating the reduced electron density around the Ni atoms that may be caused by electron donation to Pt NPs. A similar phenomenon could be found in the Fe K-edge XANES spectrum. The Fourier transformed extended X-ray absorption fine structure (EXAFS) spectra of Ni and Fe are illustrated in Fig. 3C and F, which show only one prominent peak at 2.2 Å corresponding to metal–metal scattering paths including Ni–Ni, Fe–Fe, and Fe–Ni (37). The shift of Ni–Ni peak in FeNi@NC/Pt relative to Ni foil might arise from the lattice distortion of Ni crystal after its alloying with Fe. Noticeably, the absence of any signals for metal–oxygen coordination in both Fourier and wavelet transformed spectra (Fig. 3G–J) further confirms that both Fe and Ni are dominant by the metallic states, echoing the results of XRD and XPS.

It has been demonstrated that the chemical state of Pt has a great influence on HCHO oxidation. However, the ultra-low content of Pt in FeNi@NC/Pt restricts its detection by XPS and XAFS. As a way out, another catalyst with higher Pt loading (referred to as FeNi@NC/Pt-H) was fabricated according to a similar procedure except increasing the dosage of H_2PtCl_6 during preparation. The actual Pt content of FeNi@NC/Pt-H was determined to be 0.5463 wt.% by ICP-AES, behaving the similar Pt utilization (77.7%) to that of FeNi@NC/Pt. The identical XRD pattern of FeNi@NC/Pt-H to its support indicates that the deposition of Pt NPs has no influence on the crystal structure of FeNi alloy (Fig. S14A). TEM images further demonstrate that the elevated Pt loading does not induce the agglomeration and size increase of Pt NPs (Fig. S14B–E). More importantly, FeNi@NC/Pt-H possesses a catalytic activity (94%) resembling that of FeNi@NC/Pt toward HCHO removal (Fig. S15). These results verify the advantage of FeNi@NC to evenly immobilize Pt NPs, making it rational to conduct the XPS measurement over FeNi@NC/Pt-H for elucidating the valence state of Pt. From the survey spectra and the partially enlarged one, we can see an evident Pt 4f signal adjacent to the Ni 3p peak after Pt loading (Fig. S14F and G). The high-resolution Pt 4f spectrum could be deconvoluted into three pairs of peaks at 71.5/74.9, 72.9/76.3, and 74.4/78.0 eV, corresponding to Pt^0, Pt^{2+}, and Pt^{4+}, respectively (Fig. S14H) (5, 38). Considering that Pt^0 is generally recognized as an active site for O_2 activation, the molar ratio of $Pt^0/(Pt^0 + Pt^{2+} + Pt^{4+})$ is determined (67.6%), which is higher than that of the reported Pt-based catalysts prepared by using similar methods and suggests that the majority of Pt species is in metallic state (39). The absence of Cl from XPS data for both FeNi@NC/Pt and FeNi@NC/Pt-H further confirms the anchoring of Pt NPs, rather than adsorption of $PtCl_6^{2-}$, on FeNi@NC support.

Electronic metal–support interaction

The electronic interaction between FeNi@NC and Pt NPs was further discussed from the interfacial electron exchange between metal species (Pt or FeNi) and N-doped carbon. It has been manifested that electrons could transfer spontaneously from TMs (such as Fe, Co, Ni, and their alloys) to the N-doped carbon once they contact, owing to the lower work function (Φ) of the former (18). In contrast, Pt, possessing the highest Φ among all metal elements, would attract electrons from the N-doped carbon (40). Therefore, it is rational to speculate that electrons can transfer from FeNi alloys to NC, especially pyridinic N, owing to its tendency to accept the transferred electrons (19, 20), whereas electron withdrawing from NC to Pt NPs would occur after the deposition of Pt on FeNi@NC (Fig. 4A) (21), accompanied by the

decreased electron density surrounding pyridinic N. As shown in Fig. 4B, both the high-resolution N 1s spectra of FeNi@NC and FeNi@NC/Pt contain three peaks at around 398.8, 401.1, and 403.6 eV, which are attributed to the pyridinic-N, graphitic-N, and oxidic-N species, respectively (41). Indeed, the peak of pyridinic-N in FeNi@NC/Pt shifts to a higher binding energy relative to FeNi@NC, suggesting a reduced electron density around pyridinic-N after loading of Pt due to the electron transfer from FeNi@NC to Pt. The increased Φ value after Pt stabilization onto FeNi@NC further confirms the electron donation from support to Pt (Fig. S16). Consequently, an electron flow direction from FeNi alloys to Pt NPs via NC was revealed, ultimately enriching the electron density of Pt NPs. Then, density functional theory (DFT) calculations were employed to analyze the electronic interaction between Pt and the support using two comparable models, one incorporating FeNi alloy and the other without. The model representing carbon-encapsulated FeNi alloy (referred to as FeNi@NC) features a graphene layer integrated with $Fe_{22}Ni_{33}$. Within this model, one nitrogen atom was introduced into the graphene layer to simulate N-doped carbon (N_1C_{71}). The Ni/Fe molar ratio (1.5) was determined based on ICP-AES data (Table S2). To mimic the FeNi@NC/Pt configuration (Fig. S1A and B), a Pt_4 cluster was incorporated onto the graphene layer of the FeNi@NC model. Additionally, a Pt_4 cluster was integrated into the N_1C_{71} model (referred to as NC/Pt) for comparative analysis (Fig. S1C and D). Examination of the positive Bader charge on Pt_4 in both FeNi@NC and NC configurations reveals electron transfer from the support to Pt (Fig. 4C). Notably, Pt_4 on FeNi@NC exhibited a significantly larger charge of 0.09, indicative of electron donation from FeNi to Pt, with NC acting as a mediator. Furthermore, the results from differential charge density analysis reveal a more pronounced charge redistribution within FeNi@NC/Pt when compared with NC/Pt (insets in Fig. 4C), providing additional support for the aforementioned conclusion.

Furthermore, the properties of the oxygen species were analyzed to explore the promotion effect of EMSI between FeNi@NC and Pt on oxygen activation. The high-resolution O 1s spectra of FeNi@NC and FeNi@NC/Pt display three peaks at 530.4, 531.6, and 533.3 eV, which are ascribed to the metal–oxygen bond correlated with surface oxidation of FeNi alloys, surface chemisorbed oxygen (O_{ads}) or C=O on carbon matrix, and the physically adsorbed H_2O or CO_3^{2-}, respectively (Fig. 4D) (42–44). The C 1s spectra could be deconvoluted into sp^2 C=C, C=N, and C=O at around 284.7, 285.6, and 286.5 eV, respectively, further revealing the existence form of carbon- and oxygen-containing groups (Fig. 4D) (25, 27). It is clear to see that the peak intensity of O_{ads}/C=O in FeNi@NC/Pt is higher than that in FeNi@NC. Given the importance of O_{ads} in room-temperature HCHO oxidation, the molar ratios of $O_{O_{ads}/C=O}/O_{total}$ and $C_{C=O}/C_{total}$ are calculated based on XPS data to evaluate the variation in O_{ads} content. As listed in Table 1, the $O_{O_{ads}/C=O}/O_{total}$ value increases obviously after Pt loading, while the $C_{C=O}/C_{total}$ value almost keeps constant, suggesting that the deposition of Pt NPs promotes the generation of O_{ads}. In addition, H_2 temperature-programmed reduction (H_2-TPR) was performed to assess the redox property (Fig. 4E). FeNi@NC displays an evident reduction peak at 290 °C, which may correspond to the reduction of surface oxides on FeNi alloys or oxygen-containing groups on carbon matrix. FeNi@NC/Pt exhibits a stronger reduction peak at 266 °C, which might be due to the increased number of O_{ads} generated by Pt NPs (45). The negative shift of this reduction peak may be caused by hydrogen spillover from Pt to FeNi@NC, implying a strong interaction between them (6). To sum up, the combined results of XPS, XAFS, ultraviolet photoemission spectroscopy, DFT
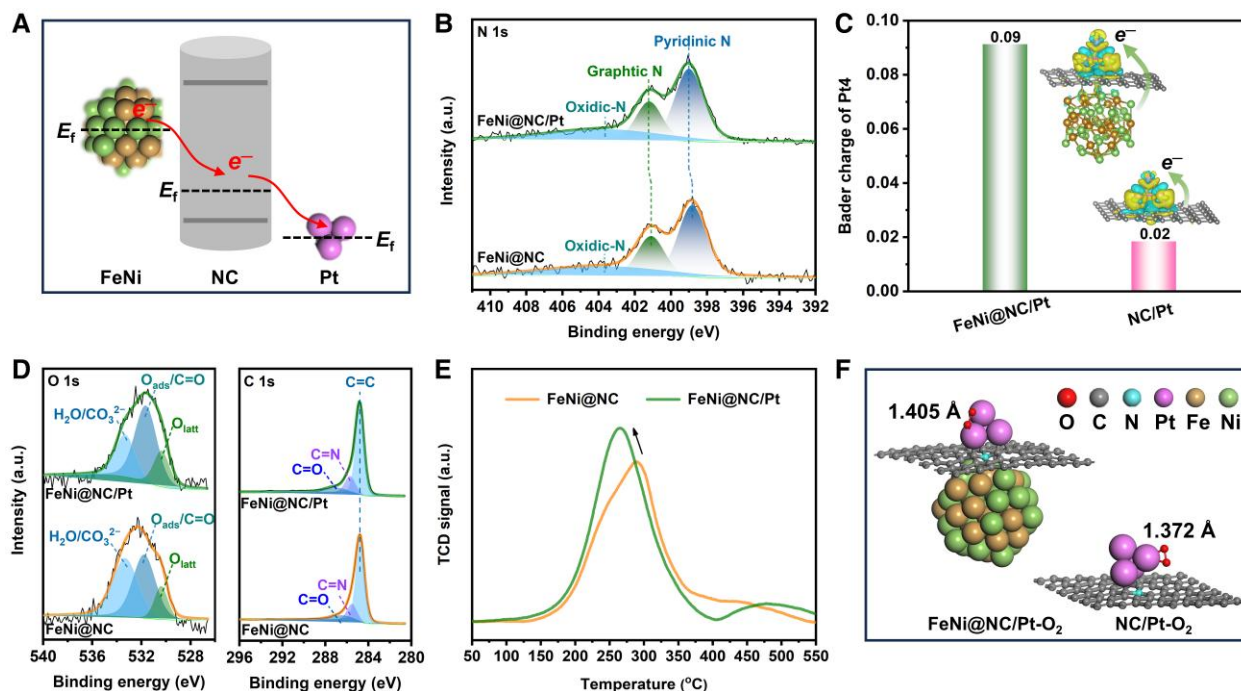
Fig. 4. Electron transfer and oxygen activation. A) Schematic illustration of electron flow direction driven by work function difference after merging the FeNi alloy, NC, and Pt, where E_f represents the Fermi energy. B) High-resolution XPS spectrum of N 1s for FeNi@NC and FeNi@NC/Pt. C) Bader charge of Pt_4 cluster on graphene layer integrating FeNi alloy or not. Insets: the differential charge density of FeNi@NC/Pt and NC/Pt, where yellow and blue regions represent electron increment and depletion, respectively. D) High-resolution O 1s and C 1s XPS spectra of FeNi@NC and FeNi@NC/Pt, respectively. E) H_2-TPR profiles of the corresponding samples. F) The favorable adsorption configurations of O_2 on the surface of Pt in FeNi@NC/Pt and NC/Pt models.

calculations, and H_2-TPR reveal the electronic interaction between Pt and FeNi@NC, which induces the intensified electron density on Pt NPs, thereby promoting oxygen activation.

Electron spin resonance (ESR) measurements were further performed to identify the types of reactive oxygen species (ROS). FeNi@NC possesses a strong ability toward O_2 activation and $\bullet O_2^-$ production, while the loading of Pt weakens the $\bullet O_2^-$ signal (Fig. S17A) (46). In contrast, CB/Pt exhibits a slightly stronger $\bullet O_2^-$ signal compared with CB (Fig. S17B). These results indicate that there must be other types of ROS induced by the electron-rich Pt NPs in FeNi@NC/Pt, despite the inherent ability of Pt for O_2 activation via a single-electron reduction to form $\bullet O_2^-$. However, the possible transformation of $\bullet O_2^-$ to $\bullet OH$ was excluded due to the absence of a characteristic signal assigned to $\bullet OH$ over FeNi@NC, FeNi@NC/Pt, and CB/Pt (Fig. S17C). Subsequently, DFT calculations were employed to investigate the distinct adsorption configurations of O_2 on Pt_4 within the FeNi@NC/Pt and NC/Pt models (Figs. 4F and S18). The calculated adsorption energy of O_2 (E_{ads}) and length of the O–O bond were acquired (Table S3). Based on E_{ads} values, two favorable adsorption configurations for O_2 on Pt_4 of FeNi@NC/Pt (denoted as I2 and I3) were identified. Notably, the bond length of O_2 adsorbed at the bridge site, positioned between two neighboring Pt atoms (I3), is significantly longer compared with the lengths observed in other configurations and the formed $\bullet O_2^-$ (1.35 Å) (47). This observation suggests the potential dissociation of chemisorbed O_2 by FeNi@NC/Pt. For the NC/Pt model, the most favorable adsorption configuration of O_2 was identified as a side-on mode on the Pt atom (II5). Notably, the bond length of the adsorbed O_2 on FeNi@NC/Pt (1.405 Å) is longer than that on NC/Pt (1.372 Å), indicating the superior ability of FeNi@NC/Pt to activate and dissociate molecular O_2 by weakening the O–O bond, as illustrated in Fig. 4F. This phenomenon can be

attributed to the easy occupation of the antibonding states of O_2 by the abundant electrons on Pt in the FeNi@NC/Pt model. Consequently, the resulting reactive O* atoms, potentially in the form of Pt–O*, are more inclined to participate in the HCHO oxidation reaction.

Moreover, the essential role of FeNi alloy in intensifying the electron density of Pt NPs was investigated by acid leaching of FeNi@NC (FeNi@NC-H^+) followed by Pt loading (FeNi@NC-H^+/Pt). It is clear to see that the FeNi@NC-H^+ support exhibits a significant attenuation in the intensity of diffraction peaks assigned to FeNi alloy and possesses the larger S_{BET} and pore volume relative to FeNi@NC (Figs. S19A and S20 and Table S4), implying that the FeNi NPs could be removed effectively through acid leaching, whereas the morphological structure remains unchanged (Fig. S19B). After loading of Pt, the ultrafine Pt particles with legible lattice fringe could be observed in FeNi@NC-H^+/Pt (Fig. S19C–F), accompanied by the slight decrease in surface area and pore volume. The evident pores could also be observed in the TEM images, further confirming the leaching of FeNi. In addition, the almost equal molar ratios of Ni/Fe before and after acid leaching indicate the simultaneous removal of Fe and Ni, thus excluding the probable influence of Ni/Fe ratio on electron-donating ability of FeNi alloy (Table S2). Then, the catalytic activity of FeNi@NC/Pt and FeNi@NC-H^+/Pt toward HCHO oxidation was evaluated (Fig. S21). Both the HCHO removal efficiency and generated CO_2 of FeNi@NC-H^+/Pt are much lower than those of FeNi@NC/Pt despite the approximate Pt loading (Table S2), suggesting that the partial removal of the embedded FeNi alloys is detrimental to HCHO degradation owing to the deficiency in electron acquisition by Pt NPs. Subsequently, another reference catalyst was prepared according to a similar procedure with FeNi@NC/Pt except for the addition of H_2PtCl_6 (FeNi@NC-Re). As expected, no improvement
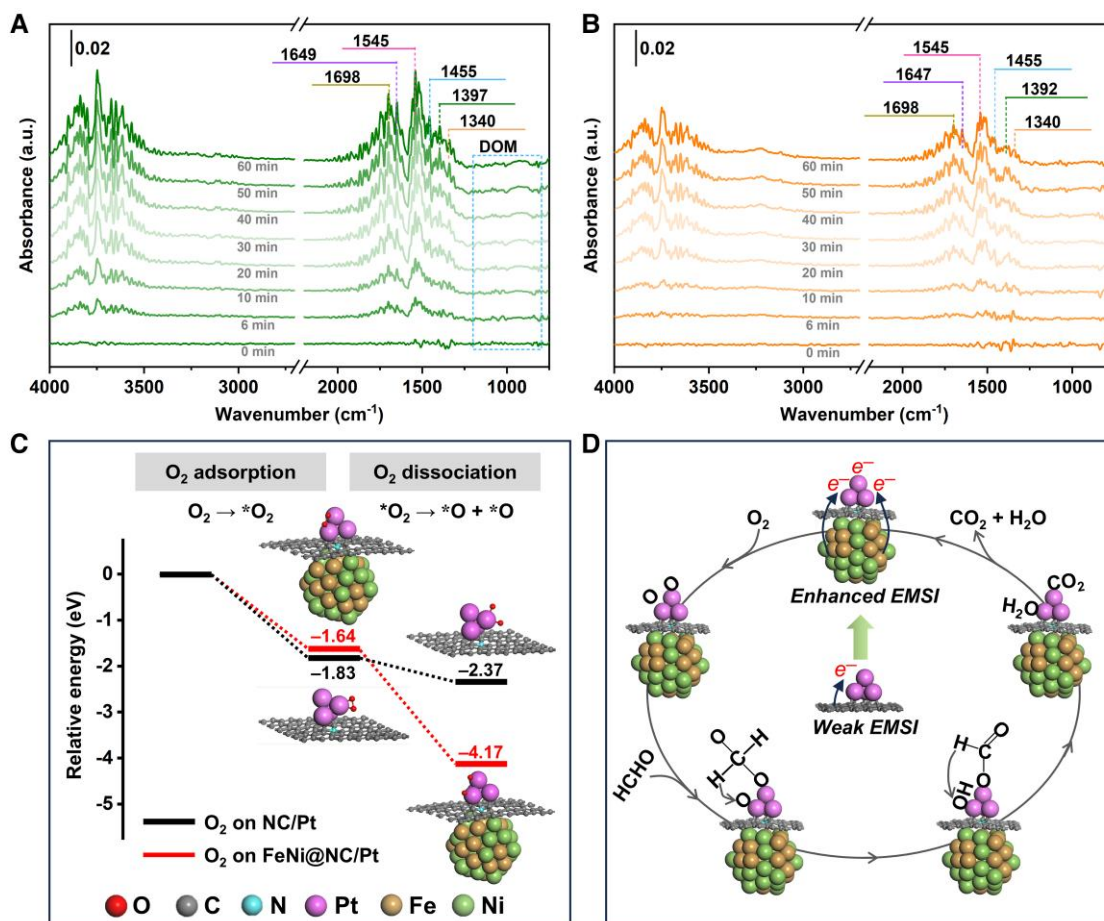
Fig. 5. In situ DRIFT spectra and proposed mechanism. In situ DRIFT spectra of A) FeNi@NC/Pt and B) FeNi@NC exposed to reactant gas containing HCHO for up to 60 min at room temperature. C) Energy profiles of O_2 adsorption and dissociation on FeNi@NC/Pt (red) and NC/Pt (black). D) Reaction mechanism of HCHO oxidation facilitated by the enhanced EMSI effect over FeNi@NC/Pt (*O_2 represents the adsorbed O_2 molecule).

in catalytic activity is obtained over FeNi@NC-Re compared with FeNi@NC (Fig. S22), suggesting that the sole reduction of support does not contribute to HCHO abatement. These results manifest that both FeNi alloys and Pt NPs are indispensable to HCHO oxidation in this novel catalyst system. Therefore, the EMSI between FeNi@NC and Pt plays a decisive role in HCHO degradation, during which oxygen activation is facilitated by the electron-rich Pt NPs.

Reaction mechanism of HCHO oxidation

The reaction mechanism of HCHO oxidation was investigated, and in situ diffuse reflectance infrared Fourier transform (DRIFT) spectroscopy was employed to analyze the process at room temperature. Figure 5A displays the characteristic peaks of intermediate species observed during HCHO oxidation over FeNi@NC/Pt. Specifically, the vibrational peaks at 1,340 and 1,545 cm^{-1} are assigned to the symmetric and asymmetric stretching modes of the –COO^- group ($v_s(COO^-)$ and $v_{as}(COO^-)$), respectively (6, 48). The signal at 1,698 cm^{-1} is attributed to the $v_s(C=O)$ mode of formate species (49). Additionally, the signal at 1,397 cm^{-1} is assigned to the $\delta(CH)$ mode of formate species (50). The weak vibrational peaks related to dioxymethylene (DOM) also could be detected at 1,455 cm^{-1} and the range of 800–1,200 cm^{-1} (51, 52). The vibrational peak at 1,649 cm^{-1} could be attributed to the adsorbed H_2O (45). These results suggest that HCHO can be oxidized into CO_2, with formate species identified as the most important intermediate

product (Fig. S23A). In the case of FeNi@NC, although most of the signals assigned to formate species were detected, the peak intensity was relatively weaker (Figs. 5B and S23B). Combined with the results of HCHO removal and ESR testing, it can be concluded that the formate species formed over FeNi@NC cannot be fully decomposed, and they occupy the active sites, thereby inhibiting the subsequent oxidation of HCHO. This observation further indicates that •O_2^- generated by FeNi@NC is not the primary ROS during HCHO oxidation. Conversely, the electron-rich Pt, induced by the enhanced EMSI effect between FeNi@NC and Pt, can efficiently activate O_2 to produce reactive O* atoms. As revealed in Fig. 5C, O_2 is adsorbed less strongly on FeNi@NC/Pt, followed by dissociation into two O* atoms more easily than that on NC/Pt. The O* atoms readily react with HCHO to form DOM, which subsequently transforms into formate species, leading to the eventual formation of the end products, CO_2 and H_2O (Fig. 5D). Importantly, this process releases the active sites for the continuous oxidation of HCHO.

Discussion

In conclusion, a novel supported Pt catalyst was developed by combining ultrafine Pt NPs with FeNi@NC to enhance molecular oxygen activation. The interwoven CNT network within FeNi@NC provided a distinct advantage in increasing the Pt source utilization. Remarkably, efficient oxidation of formaldehyde was achieved

even with ultra-low Pt loading (<0.035 wt.%) at room temperature, surpassing previous Pt-based catalysts. Multiple characterizations and DFT calculations unveiled a directional electron transfer from FeNi alloy to Pt mediated by graphitized carbon, driven by the unique EMSI effect between FeNi@NC and Pt. This charge transfers endowed Pt with electron-rich properties, enhancing O_2 activation with elongation of O–O bond, ultimately leading to the deep oxidation of formaldehyde to CO_2. This study presents a promising strategy for designing efficient Pt catalysts on nonoxide supports for the catalytic degradation of air pollutants.

Materials and methods

Additional details regarding the Materials and Methods are given in Supplementary material.

Material fabrication

Before preparing the supported noble metal catalysts, FeNi@NC was fabricated through the high-temperature pyrolysis of the mixed $Ni_3[Fe(CN)_6]_2$ and $g-C_3N_4$ precursors. First, $Ni_3[Fe(CN)_6]_2$ was synthesized through a facile self-assembly reaction of $NiCl_2$ and $K_3[Fe(CN)_6]$ in aqueous solution at room temperature. $g-C_3N_4$ was prepared by calcining melamine at 550 °C for 2 h in the muffle furnace. Then, 0.8 g of $Ni_3[Fe(CN)_6]_2$ and 1.2 g of $g-C_3N_4$ were ground in an agate mortar for 20 min to acquire their uniform mixtures, followed by pyrolyzing at 750 °C for 2 h under nitrogen atmosphere to obtain the black FeNi@NC powder. The detailed experimental process for synthesis of $Ni_3[Fe(CN)_6]_2$ is presented in Supplementary material. Subsequently, FeNi@NC was used as support to stabilize Pt NPs through an oscillation-assisted reduction pathway. Specifically, 0.17 g of FeNi@NC was dispersed in 6 mL H_2O through ultrasonication to obtain a homogeneous suspension. Then, a certain volume of H_2PtCl_6 solution (2 mg mL^{-1}) was diluted into 4 mL, followed by adding into the above suspension during oscillation and keeping for 1 h. Afterward, the freshly prepared $NaBH_4$ (0.1 mol L^{-1}) and NaOH (0.5 mol L^{-1}) aqueous solution (2 mL) was utilized to reduce $PtCl_6^{2-}$ to obtain the FeNi@NC/Pt catalyst after centrifugation and drying. FeNi@NC/Pt in this study refers to the Pt loading of 0.0694 wt.% unless otherwise stated. For comparison, CB and Fe@NC were used to deposit Pt NPs according to a similar procedure and denoted as CB/Pt and Fe@NC/Pt, respectively.

Structural characterizations

The experimental details of catalyst characterizations and DFT calculations are presented in Supplementary material.

Catalytic activity evaluation

The HCHO oxidation activity was evaluated using a fixed-bed reactor, where 0.1 g of catalyst (40–60 meshes) was sandwiched by silica wool in a stainless steel tube ($\Phi = 6$ mm) during each test. The initial concentration of HCHO was determined to be 100 ppm by passing an air flow through the formaldehyde solution (37 wt.%) in a stainless steel container at 15 °C, while the RH was controlled by air flow through the water tank. Gas hourly space velocity was determined to be 60,000 mL g^{-1} h^{-1} by adjusting the total flow rate (100 mL min^{-1}) with mass flow meters. The concentrations of HCHO and CO_2 during HCHO oxidation were monitored by an INNOVA 1412i photoacoustic gas monitor (LumaSense Technologies, Inc., Denmark) in real time, with the detection limits of 0.04 and 5.1 ppm for HCHO and CO_2,

respectively. HCHO removal efficiency (η, %) was calculated according to the following equation:

$$\eta = (1 - [HCHO]_{out}/[HCHO]_{in}) \times 100\%$$

where $[HCHO]_{in}$ and $[HCHO]_{out}$ represent the initial and real-time concentration of HCHO (ppm), respectively. The recycling tests were carried out by repeating the HCHO removal testing over FeNi@NC/Pt five times at identical conditions.

Supplementary Material

Supplementary material is available at *PNAS Nexus* online.

Author Contributions

Y.H. supervised the project. D.Z. and Y.H. conceived and designed the experiments and co-wrote the manuscript. D.Z. performed the key experiments and analyzed the results. X.S. and W.P. performed the materials simulations. D.Z., R.L., Z.W., J.C., and S.L. discussed the data.

Data Availability

All data are included in the article and Supplementary material.

References

1 Gan T, *et al.* 2021. Electron donation of non-oxide supports boosts O_2 activation on nano-platinum catalysts. *Nat Commun.* 12(1): 2741.

2 Huang X, *et al.* 2022. Au-Pd separation enhances bimetallic catalysis of alcohol oxidation. *Nature.* 603(7900):271–275.

3 Chong L, *et al.* 2018. Ultralow-loading platinum-cobalt fuel cell catalysts derived from imidazolate frameworks. *Science.* 362(6420):1276–1281.

4 Li D, *et al.* 2023. New insights into the catalytic mechanism of VOCs abatement over Pt/beta with active sites regulated by zeolite acidity. *Appl Catal B Environ.* 334:122811.

5 Huang Z, *et al.* 2022. Highly efficient oxidation of propane at low temperature over a Pt-based catalyst by optimization support. *Environ Sci Technol.* 56(23):17278–17287.

6 Zhuo Y, *et al.* 2023. Synergetic modulation of molecular oxygen activation and surface acidity/basicity on defective M/UiO-66m (M = Pt, Pd) for advanced oxidation of gaseous formaldehyde at room temperature. *Appl Catal B Environ.* 333:122789.

7 Di Z, *et al.* 2023. Principle on selecting the coordination ligands of palladium precursors encapsulated by zeolite for an efficient purification of formaldehyde at ambient temperature. *Environ Sci Technol.* 57(43):16641–16652.

8   Ahmad W, *et al.* 2023. Metal-anchoring, metal oxidation-resistance, and electron transfer behavior of oxygen vacancy-rich TiO_2 in supported noble metal catalyst for room temperature HCHO conversion. *Chem Eng J.* 467:143412.

9   He M, Cao Y, Ji J, Li K, Huang H. 2021. Superior catalytic performance of Pd-loaded oxygen-vacancy-rich TiO_2 for formaldehyde oxidation at room temperature. *J Catal.* 396:122–135.

10   Guo J, Lin C, Jiang C, Zhang P. 2019. Review on noble metal-based catalysts for formaldehyde oxidation at room temperature. *Appl Surf Sci.* 475:237–255.

11   Zhang Z, *et al.* 2022. Effect of hydroxyl groups on metal anchoring and formaldehyde oxidation performance of Pt/Al_2O_3. *Environ Sci Technol.* 56(15):10916–10924.

12   Li Y, Zhang Y, Qian K, Huang W. 2022. Metal–support interactions in metal/oxide catalysts and oxide–metal interactions in oxide/metal inverse catalysts. *ACS Catal.* 12(2):1268–1287.

13   Xiao M, Yu X, Guo Y, Ge M. 2022. Boosting toluene combustion by tuning electronic metal-support interactions in in situ grown $Pt@Co_3O_4$ catalysts. *Environ Sci Technol.* 56(2):1376–1385.

14   Zhang J, *et al.* 2021. Tuning metal-support interaction of $Pt-CeO_2$ catalysts for enhanced oxidation reactivity. *Environ Sci Technol.* 55(24):16687–16698.

15   Wang L, *et al.* 2023. Electron donation promotes the dual activation of lattice oxygen and molecular oxygen: the $Pt-Pd/CeO_2$ catalyst efficiently catalyzes toluene. *J Catal.* 428:115133.

16   Huang H, *et al.* 2021. Controllable synthesis of grain boundary-enriched Pt nanoworms decorated on graphitic carbon nanosheets for ultrahigh methanol oxidation catalytic activity. *J Energy Chem.* 57:601–609.

17   Wang CY, *et al.* 2021. A nonoxide catalyst system study: alkali metal-promoted Pt/AC catalyst for formaldehyde oxidation at ambient temperature. *ACS Catal.* 11(1):456–465.

18   Yu L, Deng D, Bao X. 2020. Chain mail for catalysts. *Angew Chem Int Ed Engl.* 59(36):15294–15297.

19   Wang J, *et al.* 2020. Constructing Co@N-doped graphene shell catalyst via Mott-Schottky effect for selective hydrogenation of 5-hydroxylmethylfurfural. *Appl Catal B Environ.* 263:118339.

20   Wei Q, Wang J, Shen W. 2021. Atomically dispersed $Fe^{\delta+}$ anchored on nitrogen-rich carbon for enhancing benzyl alcohol oxidation through Mott-Schottky effect. *Appl Catal B Environ.* 292:120195.

21   Sun LH, *et al.* 2021. Heterojunction-based electron donors to stabilize and activate ultrafine Pt nanoparticles for efficient hydrogen atom dissociation and gas evolution. *Angew Chem Int Ed Engl.* 60(49):25766–25770.

22   Wang Y, *et al.* 2021. Electron penetration triggering interface activity of Pt-graphene for CO oxidation at room temperature. *Nat Commun.* 12(1):5814.

23   Liang S, Jiang Q, Wang Q, Liu Y. 2021. Revealing the real role of nickel decorated nitrogen-doped carbon catalysts for electrochemical reduction of CO_2 to CO. *Adv Energy Mater.* 11(36):2101477.

24   Sun H, *et al.* 2023. Directional electronic tuning of Ni nanoparticles by interfacial oxygen bridging of support for catalyzing alkaline hydrogen oxidation. *Proc Natl Acad Sci U S A.* 120(45):e2308035120.

25   Song Q, *et al.* 2019. Enhanced electrocatalytic performance through body enrichment of Co-based bimetallic nanoparticles in situ embedded porous N-doped carbon spheres. *Small.* 15(44):1903395.

26   Zhang Q, *et al.* 2021. N, P doped carbon nanotubes confined WN-Ni Mott-Schottky heterogeneous electrocatalyst for water splitting and rechargeable zinc-air batteries. *Appl Catal B Environ.* 298:120511.

27   Li M, *et al.* 2023. Synthesis of three-dimensional (3D) hierarchically porous iron-nickel nanoparticles encapsulated in boron and nitrogen-codoped porous carbon nanosheets for accelerated water splitting. *J Colloid Interface Sci.* 652:758–769.

28   Yao Y, *et al.* 2022. Rational regulation of Co-N-C coordination for high-efficiency generation of $^1O_2$ toward nearly 100% selective degradation of organic pollutants. *Environ Sci Technol.* 56(12):8833–8843.

29   Xiao M, *et al.* 2023. Ni-doping-induced oxygen vacancy in $Pt-CeO_2$ catalyst for toluene oxidation: enhanced catalytic activity, water-resistance, and SO_2-tolerance. *Appl Catal B Environ.* 323:122173.

30   Feng Y, *et al.* 2022. Boosting catalytic stability for VOCs removal by constructing PtCu alloy structure with superior oxygen activation behavior. *J Hazard Mater.* 439:129612.

31   Wu X, *et al.* 2023. Pt single atoms and defect engineering of TiO_2-nanosheet-assembled hierarchical spheres for efficient room-temperature HCHO oxidation. *J Hazard Mater.* 454:131434.

32   Liu X, *et al.* 2023. Room temperature removal of high-space-velocity formaldehyde boosted by fixing Pt nanoparticles into Beta zeolite framework. *J Hazard Mater.* 458:131848.

33   Sun S, *et al.* 2022. Engineering stable Pt nanoclusters on defective two-dimensional TiO_2 nanosheets by introducing SMSI for efficient ambient formaldehyde oxidation. *Chem Eng J.* 435:135035.

34   He J, *et al.* 2023. Ni-Mn spinel aerogel catalysts with adsorption induced superior activity for low-temperature toluene oxidation. *Chem Eng J.* 454:140039.

35   Zhang Y, *et al.* 2021. Effect of the A-site cation over spinel AMn_2O_4 ($A = Cu^{2+}, Ni^{2+}, Zn^{2+}$) for toluene combustion: enhancement of the synergy and the oxygen activation ability. *Fuel.* 288:119700.

36   Soltan WB, *et al.* 2022. Discovering the key role of MnO_2 and CeO_2 particles in the Fe_2O_3 catalysts for enhancing the catalytic oxidation of VOC: synergistic effect of the lattice oxygen species and surface-adsorbed oxygen. *Sci Total Environ.* 819:152844.

37   Li J, *et al.* 2023. Enhancing the activity of FeNi bimetallic electrocatalysts on overall water splitting by Nd_2O_3-induced FeNi lattice contraction. *J Energy Chem.* 87:42–50.

38   Fan J, Sun Y, Fu M, Li J, Ye D. 2022. Modulate the metal support interactions to optimize the surface-interface features of Pt/CeO_2 catalysts for enhancing the toluene oxidation. *J Hazard Mater.* 424:127505.

39   Sun H, Yu X, Guo Y, Deng J, Ge M. 2022. Achieving efficient toluene oxidation over metal–organic framework-derived $Pt/CeO_2-Co_3O_4$ catalyst. *Appl Surf Sci.* 591:153225.

40   Wu P, *et al.* 2019. Promoting Pt catalysis for CO oxidation via the Mott-Schottky effect. *Nanoscale.* 11(40):18568–18574.

41   Qi D, *et al.* 2020. Engineering atomic sites via adjacent dual-metal sub-nanoclusters for efficient oxygen reduction reaction and Zn-air battery. *Small.* 16(48):2004855.

42   Pan Y, *et al.* 2021. Unveiling the nature of room-temperature O_2 activation and $O_2^{\bullet-}$ enrichment on MgO-loaded porous carbons with efficient H_2S oxidation. *ACS Catal.* 11(10):5974–5983.

43   Li Y, Dong T, Huang P, Ji J, Huang H. 2024. Efficient HCHO oxidation at room temperature via maximizing catalytic sites in 2D coralloid $\delta-MnO_2@GO$. *Appl Catal B Environ.* 341:123322.

44   Zhao Q, *et al.* 2023. Boosting the catalytic performance of volatile organic compound oxidation over platelike $MnO_2/CoAlO$ catalyst by weakening the Co–O bond and accelerating oxygen activation. *ACS Catal.* 13(2):1492–1502.

45   Ji J, Lu X, Chen C, He M, Huang H. 2020. Potassium-modulated $\delta-MnO_2$ as robust catalysts for formaldehyde oxidation at room temperature. *Appl Catal B Environ.* 260:118210.

46   Zou N, *et al.* 2019. Electrothermal regeneration by Joule heat effect on carbon cloth based MnO_2 catalyst for long-term formaldehyde removal. *Chem Eng J.* 357:1–10.

47 Montemore MM, van Spronsen MA, Madix RJ, Friend CM. 2018. O_2 activation by metal surfaces: implications for bonding and reactivity on heterogeneous catalysts. *Chem Rev.* 118(5): 2816–2862.

48 Rong S, He T, Zhang P. 2020. Self-assembly of MnO_2 nanostructures into high purity three-dimensional framework for high efficiency formaldehyde mineralization. *Appl Catal B Environ.* 267: 118375.

49 Liu F, *et al.* 2022. Synergy of surface sodium and hydroxyl on $NaTi_2HO_5$ nanotubes accelerating the Pt-dominated ambient HCHO oxidation. *J Hazard Mater.* 421:126769.

50 Ye J, *et al.* 2022. Hierarchical Co_3O_4-NiO hollow dodecahedron-supported Pt for room-temperature catalytic formaldehyde decomposition. *Chem Eng J.* 430:132715.

51 Vikrant K, Kim KH, Dong F, Boukhvalov DW, Choi W. 2022. Deep oxidation of gaseous formaldehyde at room-temperature by a durable catalyst formed through the controlled addition of potassium to platinum supported on waste eggshell. *Chem Eng J.* 428:131177.

52 Li R, *et al.* 2021. Improved oxygen activation over a carbon/Co_3O_4 nanocomposite for efficient catalytic oxidation of formaldehyde at room temperature. *Environ Sci Technol.* 55(6):4054–4063.